Journal of Materials Chemistry A

ROYAL SOCIETY OF CHEMISTRY

PAPER

View Article Online
View Journal | View Issue

Cite this: J. Mater. Chem. A, 2023, 11, 13783

Regulating Ru active sites by Pd alloying to significantly enhance hydrazine oxidation for energy-saving hydrogen production†

Simeng Zhao,[a] Yankai Zhang,[a] Haibo Li,[a] Suyuan Zeng,[a] Rui Li,[a] Qingxia Yao,[a] Hongyan Chen,[a] Yao Zheng *[b] and Konggang Qu *[a]

Integrating the hydrogen evolution reaction (HER) with the hydrazine oxidation reaction (HzOR) can construct a novel electrolytic system and thus accomplish energy-efficient H_2 production, which necessitates exploring excellent bifunctional electrocatalysts for the HER and HzOR. As alternatives to prohibitive and scarce Pt, alloy materials can synergistically exhibit appreciably enhanced catalytic activity, and simultaneously can be also endowed with a bifunctionality arising from the intermixed components. Herein, we facilely synthesized ultrafine RuPd alloy nanoparticles onto pretreated activated carbon (RuPd/C), which possesses improved dispersion and tailored electronic properties relative to mono-metallic samples, thus exhibiting remarkably boosted bifunctional performance for alkaline HER and HzOR. At 10 mA cm^{-2}, RuPd/C merely demands ultralow potentials of −15.3 mV for the HER and −77.9 mV for the HzOR, overmatching Pt/C. Moreover, the two-electrode cell just requires a voltage of 17.7 and 147.6 mV to afford 10 and 100 mA cm^{-2}, much superior to traditional water splitting (~2 V), displaying its immense superiority in energy saving, which can be also readily driven by a self-made direct hydrazine fuel cell and commercial solar cell with an appreciable H_2 generation of 0.85 and 0.98 mmol h^{-1}, respectively. Theoretical calculations unravel that the HER and HzOR both occur on Ru sites, which can be achieved by Pd alloying with a lower water dissociation barrier and optimized hydrogen adsorption free energy for the HER, and also improved dehydrogenation kinetics for the HzOR.

Received 14th April 2023
Accepted 17th May 2023

DOI: 10.1039/d3ta02238b

rsc.li/materials-a

1. Introduction

The overconsumption of traditional carbon-based energy leads to increasingly serious energy shortage and environmental degradation.[1] As a clean, zero-carbon and reusable secondary energy source, hydrogen is anticipated as the first choice to replace traditional fossil energy,[2–4] thus, one of the major issues is to explore clean and economical paths to produce H_2.[5] Thereinto, electrochemical overall water splitting (OWS) is the most appealing technique due to the convenient operation, zero carbon emission and high purity,[6,7] which includes the anodic oxygen evolution reaction (OER) and cathodic hydrogen evolution reaction (HER).[8–10] However, the energy-demanding and inherently slow $4e^-$ kinetics of the OER bring about huge power consumption, which is one foremost limitation in the practicability of high-efficiency OWS.[11–14] In this case, combining the HER with one low-potential half-reaction is exceedingly propitious to circumvent the aforesaid obstacles from the OER.[15–17]

Konggang Qu is an associate professor at the School of Chemistry and Chemical Engineering, Liaocheng University. He received his PhD degree in 2013 from Changchun Institute of Applied Chemistry, Chinese Academy of Science. He has worked as a postdoctoral researcher in the University of Adelaide (2014–2015). His current research interests focus on nanostructured materials for energy conversion and catalysis and understanding their reaction mechanisms.

[a]School of Chemistry and Chemical Engineering, Shandong Provincial Key Laboratory/Collaborative Innovation Center of Chemical Energy Storage & Novel Cell Technology, Liaocheng University, Liaocheng 252059, China. E-mail: qukonggang@lcu.edu.cn

[b]School of Chemical Engineering and Advanced Materials, The University of Adelaide, Adelaide 5005, SA, Australia. E-mail: yao.zheng01@adelaide.edu.au

† Electronic supplementary information (ESI) available. See DOI: https://doi.org/10.1039/d3ta02238b

Particularly, the hydrazine oxidation reaction (HzOR) features an ultralow theoretical potential (−0.33 V *vs.* RHE) and pollution-free byproduct,[18,19] and thus build a new electrolytic system of overall hydrazine splitting (OHzS), accomplishing energy-efficient H_2 generation.[20,21] Thus, the development of highly active electrocatalysts for the bifunctional HER and HzOR is compulsory.[22,23]

Conventionally, Pt-based nanomaterials still dominate in the benchmarked electrocatalysts for the HER and HzOR, but the unaffordable cost and low abundance of Pt seriously hinder its widespread application.[24] Among Pt-free noble metals, Ru and Pd both share Pt-like hydrogen bonding energy, the virtue of relatively lower cost and robust corrosion resistance that transition metals have no, and thus, can be an excellent alternative to Pt.[25–28] Although multitudes of Ru- or Pd-based electrocatalysts have been reported in recent years, a gap in electrocatalytic activity between monometallic materials (especially for Pd) with Pt remains.[27,29] Additionally, mono-component materials generally cannot meet multiple requirements in exploiting electrocatalysts for the bifunctional HER and HzOR, which both involve multistep processes under non-acidic conditions.[30] Comparatively, bimetallic alloy catalysts often exhibit markedly intensified activity relative to the mono-metallic analogues, because of the synergistic strain and/or electronic effect.[31–33] Meanwhile, the alloy can be also potentially endowed with a bifunctionality arising from the intermixed components with the well-tailored physicochemical properties.[31,34,35] On the other hand, to maximize the efficacy of catalysts, the fine dispersity of naked noble metals without capping agents is compulsory, and it can be delicately achieved by immobilizing metals on eligible carbonaceous supports, which can also afford additionally high surface area and benign electricity.[36] Therefore, exploring the simple alloying strategy is highly promising to develop advanced bifunctional electrocatalysts for the HER and HzOR, and the synergistic roles assumed by different metallic components in alloys need to be clarified.[37]

Herein, we synthesized ultrafine RuPd alloy nanoparticles loaded on oxidized activated carbon (RuPd/C) with an average size of 2.5 nm as a superior bifunctional HER and HzOR electrocatalyst. Specifically, this newly-prepared RuPd/C can achieve 10 mA cm^{-2} with a small potential of −15.3 mV for alkaline HER, surpassing Pt/C. As for the HzOR, the current densities of 10 and 400 mA cm^{-2} are obtained under working potentials of mere −77.9 and 77.2 mV, superior to most recently reported HzOR catalysts. Impressively, the two-electrode OHzS system just requires a voltage of 17.7 mV at 10 mA cm^{-2}, greatly outperforming the OWS system (1.9 V) with huge energy-efficient superiority, which can be readily driven by a DHHPFC and commercial solar cell with the H_2 yield of 0.85 and 0.98 mmol h^{-1}, respectively. Density functional theory (DFT) calculations further disclose that alloying can optimize the electronic properties of Ru, and thus effectively regulate water dissociation and the H* ad/desorption process and reduce the free energy of $N_2H_2^*$ dehydrogenation to N_2H^* in the HzOR process.

2. Experimental section

2.1. Pretreatment of commercial activated carbon

The purchased activated carbon (Cabot Vulcan XC-72R) was dispersed in 65% HNO_3, stirred at constant temperature 60 °C in an oil bath, and preoxidized for 4 h. After that, the partially oxidized activated carbon was obtained after centrifuging thrice using water. The resultant oxidized activated carbon was dried in oven at 60 °C for 12 h.

2.2. The preparation of RuPd/C

50 mg preoxidized activated carbon was sonicated in 15 mL water and then mixed with appropriate amounts of $RuCl_3$ and K_2PdCl_4 (the molar ratio of Ru and Pd is 8 : 2). 10 mL $NaBH_4$ solution (the molar ratio of $NaBH_4$ and metal is 4 : 1) was added dropwise under vigorous stirring. The mixture was kept stirring for another 2 h followed by centrifuging thrice and drying. The obtained RuPd alloy nanoparticles on activated carbon was denoted as RuPd/C and the total loading of Ru and Pd metal is 20 wt%.

2.3. The preparation of Ru/C and Pd/C

Following the same synthesis procedure of RuPd/C, Ru nanoparticles on activated carbon (Ru/C) and Pd nanoparticles on activated carbon (Pd/C) were prepared with the appropriate amount of $RuCl_3$ and K_2PdCl_4, respectively. Both the Ru and Pd contents are 20 wt%.

3. Results and discussion

3.1. Synthesis and characterization

The metallic crystal phases of the samples were assessed by X-ray diffraction (XRD). Three main signals for Pd/C at 40.1, 46.7, and 68.1° separately correspond to the (111), (200), and (220) lattice planes of Pd (JCPDS No.46-1043).[38] One peak at 42.2° of Ru/C belongs to the (002) lattice plane of Ru (JCPDS No. 06-0663).[39] Comparatively, the main diffraction peak of RuPd/C was at about 40.4° with a slight negative shift relative to Ru/C, which further confirms the existence of the RuPd alloy. Raman spectroscopy was performed to examine the carbon structure.[18,40] The intensity ratio of the D band and the G band (I_D/I_G) of the three samples all fall in between 0.97 and 0.98, suggesting the good graphitization degree of carbon and little influence on the microstructure of carbon after the loading of different metal particles on the carbon surface. Additionally, the textural properties by N_2 adsorption–desorption reveal exactly similar type-II isotherms for the three kinds of samples (Fig. 1C). The surface areas are also very close from Brunauer–Emmett–Teller (BET) analysis with a range of 160.4–178.59 m^2 g^{-1} for Pd/C, Ru/C and RuPd/C. RuPd/C also has a little smaller pore volume of 0.31 cm^3 g^{-1} than that of Pd/C (0.43 cm^3 g^{-1}) and Ru/C (0.50 cm^3 g^{-1}), all of which possess large pores with the average size range of 12.4–14.8 nm, mainly resulting from the stacked voids of particle accumulation (Table S1†).

Transmission electron microscopy (TEM) was then employed to evaluate the nanostructure of the catalysts (Fig. 1D). The

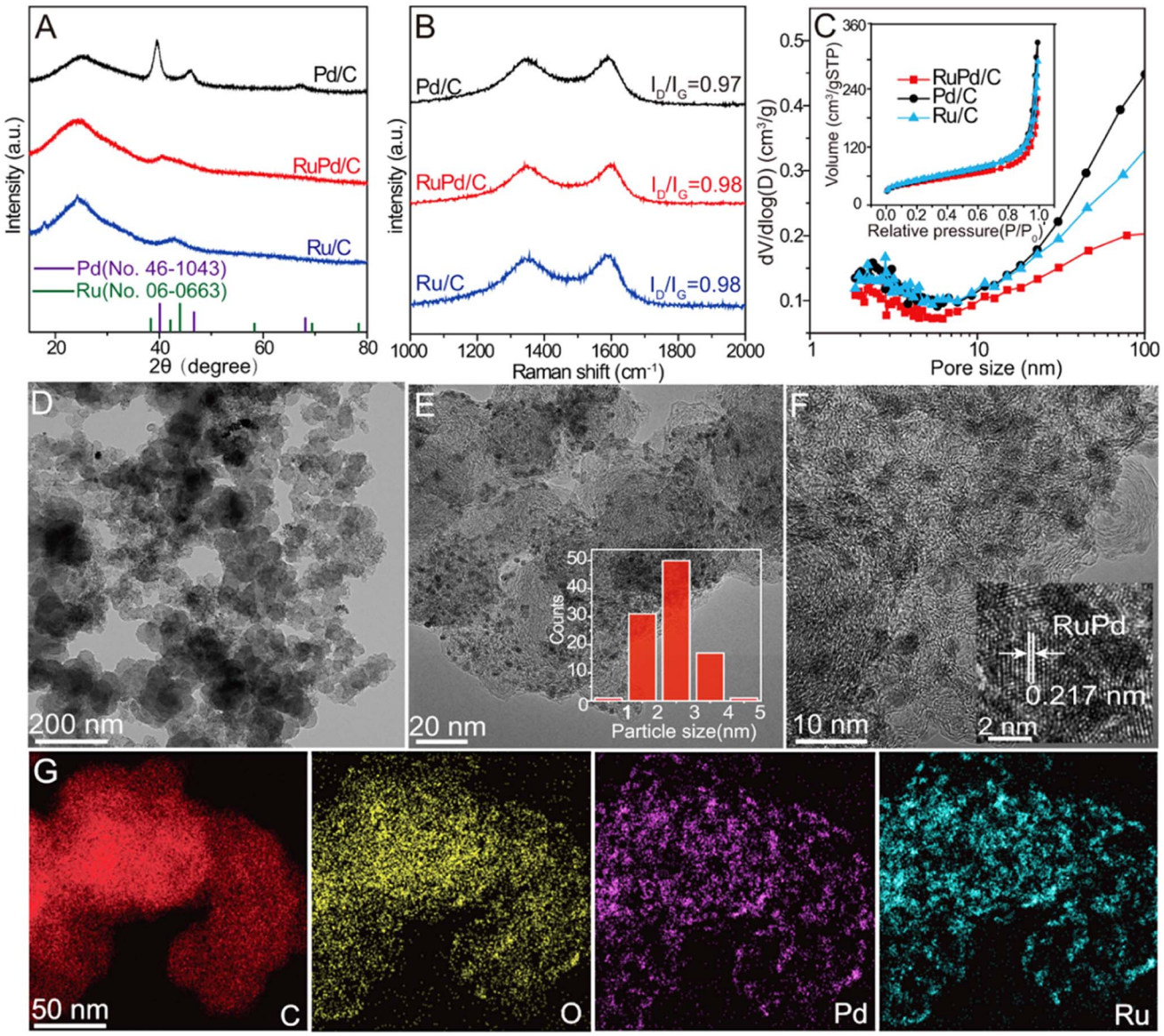

Fig. 1 (A). XRD patterns, (B) Raman spectra, (C) the pore size distribution curve and N_2 adsorption–desorption isotherm (Inset) of Pd/C, RuPd/C and Ru/C. (D–F) TEM images at different magnifications and particle size distribution (E inset) of RuPd/C. (G) TEM elemental mapping images of C, O, Pd and Ru elements in RuPd/C.

ultrafine and isolated alloy nanoparticles are distributed evenly on each quasi-spherical activated carbon, and there is no obvious aggregation of alloy particles. Additionally, the tiny RuPd alloy particles are well-dispersed and homogeneous with a mean diameter of 2.5 nm (Fig. 1E). A lattice fringe spacing of 0.217 nm was observed by high-resolution TEM (HRTEM), not belonging to any of Pd or Ru, but very close to that of the RuPd alloy (0.219 nm),[41,42] indicating the successful formation of the bimetallic RuPd alloy.[41,43,44] The elemental mapping images (Fig. 1G.) suggest that C, O, Ru and Pd elements coexist in RuPd/C with high overlapping of Ru and Pd signals. However, Pd/C possesses very uneven Pd particles with the size from about 5 nm to 30 nm (Fig. S1†). However for Ru/C, uniform Ru nanoparticles can be observed but with a relatively larger average size of 4.5 nm (Fig. S2†). These pieces of evidence indicate that alloying with Ru can effectively suppress the aggregation of the Pd moiety and facilitate the formation of well-dispersed alloy particles.[43]

The metal valence states and electron interactions can be obtained by X-ray photoelectron spectroscopy (XPS) analysis (Fig. 2 and S3†). The existence of C, O, Ru and Pd components can be observed in RuPd/C (Fig. 2A). For RuPd/C, the signals at 461.8 and 484.2 eV separately match with the binding energies of Ru^0 $3p_{3/2}$ and Ru^0 $3p_{1/2}$, while those of 465.1 and 486.6 eV belong to $3p_{3/2}$ and $3p_{1/2}$ of Ru–O bonds (Fig. 2B). Similarly, for Ru/C, the main signals at 462.1 and 484.4 eV accord with the characteristic peaks of Ru^0 $3p_{3/2}$ and Ru^0 $3p_{1/2}$ while the ones of 465.3 and 486.9 eV arise from $3p_{3/2}$ and $3p_{1/2}$ of Ru–O bonds. Likewise, the spectra of Pd 3d in RuPd/C and Pd/C both contain two sets of signals. Specifically, the $3d_{5/2}$ and $3d_{3/2}$ peaks of Pd^0

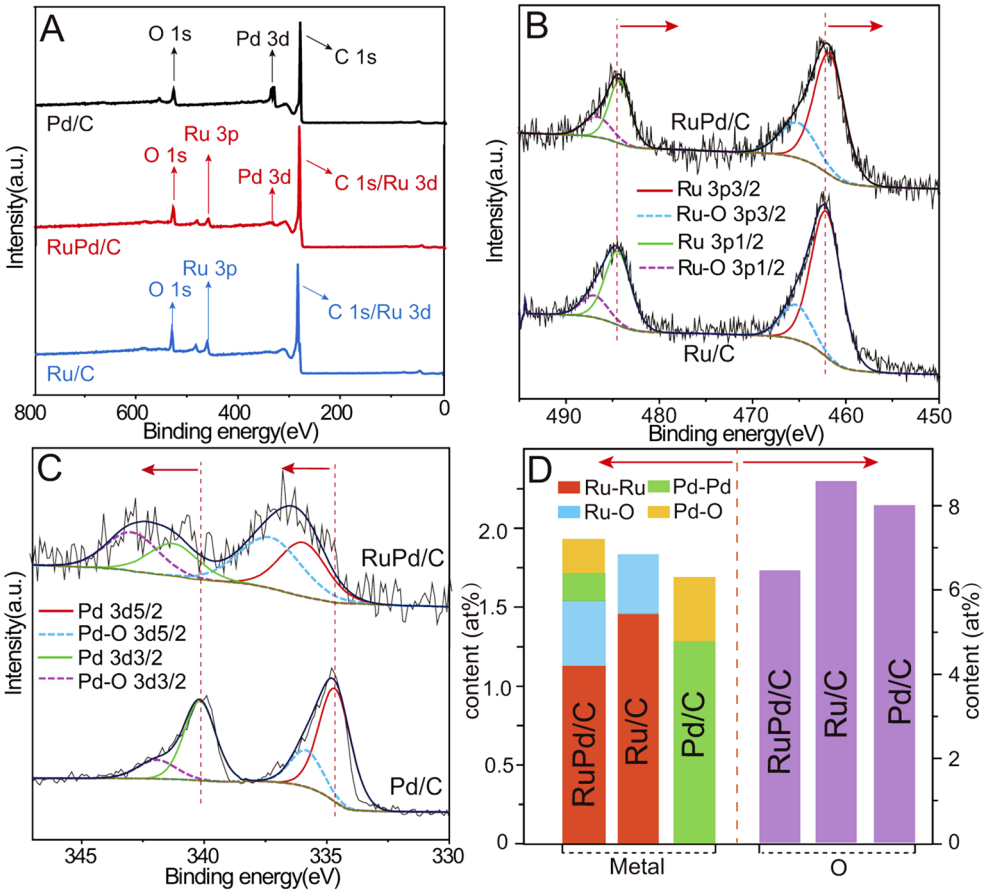

Fig. 2 (A) XPS survey scan and high-resolution XPS spectra of (B) Ru 3p of RuPd/C and Ru/C, and (C) Pd 3d of RuPd/C and Pd/C. (D) The componential comparison of metal and O on the sample surface.

are located at 336.4 and 341.3 eV together with those of Pd–O bonds at 337.3 and 342.9 eV (Fig. 2C). Comparatively, Pd/C shows the peaks of Pd^0 $3d_{3/2}$ and $3d_{5/2}$ at 340.1 and 334.7 eV, as well as those of Pd–O $3d_{3/2}$ and $3d_{5/2}$ centered at 341.9 and 336.0 eV, respectively. The metal atoms at the surface of ultrafine particles are easily oxidized due to the unsaturated coordination, accounting for the existence of Ru–O and Pd–O bonds in the alloy. Impressively, it can be observed that the peak position of Ru $3p_{3/2}$ in RuPd/C shows a negative shift (0.2–0.4 eV) compared with Ru/C. However, the characteristic peak of Pd 3d of RuPd/C has a distinct positive displacement (1.0–1.3 eV) relative to Pd/C, indicating the electron transfer from Pd to Ru due to the electronegativity difference, and these distinct shifts demonstrate that the electronic properties of metal can be tailored by alloying, consequently regulating the catalytic behaviors of metal sites during electrocatalytic processes. Fig. 2D and Table S2† present very close contents of metals and abundant O species on the surface of the three samples, which can improve the hydrophilicity of the catalysts and thus expedite the gas evolution during electrocatalysis.

3.2. Electrocatalytic HER and HzOR performance

The electrochemical activities of the catalysts for the HER were investigated in alkaline electrolytes. Detailed analyses of linear sweep voltammetry (LSV) data in Fig. 3A and B show that RuPd/C affords the lowest overpotential of 15.3 mV at 10 mA m^{-2} with the smallest Tafel slope of 47.0 mV dec^{-1}, outperforming Pt/C (18.4 mV, 63.2 mV dec^{-1}), Ru/C (29.5 mV, 68.6 mV dec^{-1}) and Pd/C (290.3 mV, 230.2 mV dec^{-1}), suggesting the best HER activity on RuPd/C. Additionally, a small overpotential of 124.3 mV was needed to afford 100 mA cm^{-2} on RuPd/C, less than that of Pt/C (144.2 mV), Ru/C (161.8 mV) and Pd/C (464.6 mV), also indicating the excellent high-current-density activity for RuPd/C. Electrochemical impedance spectroscopy (EIS) reveals a charge-transfer resistance (R_{ct}) value of (2.6 Ω) on RuPd/C, superior to that of Pt/C (8.0 Ω), Ru/C (3.0 Ω) and Pd/C (24.8 Ω), implying the fastest reaction kinetics on RuPd/C (Fig. S4A†). Furthermore, the measured current–time signal on RuPd/C presents its excellent durability for 10 h without obvious decay (Fig. 3C).

The HzOR performances of different samples were then examined in 1.0 M KOH/0.5 M N_2H_4 electrolyte. As shown in Fig. 3D, it can be observed from the LSV curve that RuPd/C merely needs ultralow potentials (−77.9 and −49.1 mV) to achieve 10 and 100 mA cm^{-2}, superior to Pt/C (134 and 233.6 mV), Ru/C (−47.3 and 142.2 mV) and Pd/C (155.4 and 339.3 mV), also overmatching recently reported Ru,[18,19,37,45,46] Rh,[47,48] Ir,[20] alloys,[23,49–53] and even self-supported materials,[3,5,54–56]

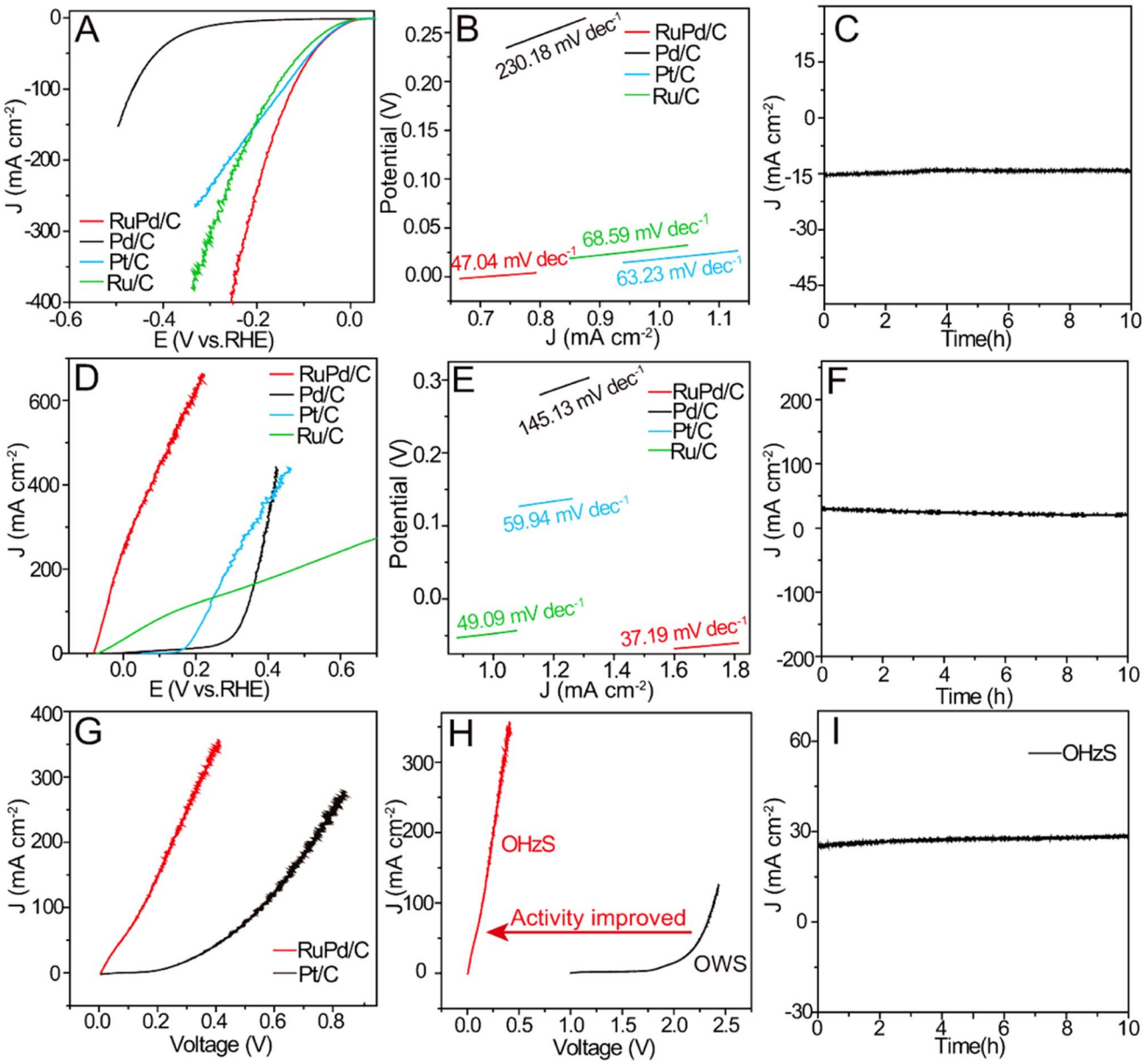

Fig. 3 (A) HER LSV curves and corresponding (B) Tafel slopes of RuPd/C, Rd/C, Pt/C and Ru/C in 1 M KOH. (C) Current density–time curve of RuPd/C during the HER process., (D) HzOR LSV curves and corresponding (E) Tafel slopes of RuPd/C, Rd/C, Pt/C and Ru/C in 1 M KOH + 0.5 M N_2H_4, and (F) Current density–time curve of RuPd/C during the HzOR process. (G) Two-electrode OHzS curves using RuPd/C and Pt/C as bifunctional electrodes. (H) LSV curves of OHzS and OWS on RuPd/C. (I) OHzS stability test of RuPd/C.

demonstrating the exceptionally superior HzOR activity on RuPd/C. These reflect the significantly enhanced HzOR activity by alloying and the great advantage in replacing the OER for energy-efficient H_2 generation. Moreover, RuPd/C also shows the smallest Tafel slope (37.2 mV dec^{-1}) and R_{ct} value (1.8 Ω), in comparison with those of Pt/C (59.9 mV dec^{-1}, 3.8 Ω), Ru/C (49.1 mV dec^{-1}, 9.2 Ω) and Pd/C (145.1 mV dec^{-1}, 121.9 Ω), demonstrating the exceptional reaction kinetics of RuPd/C toward the HzOR (Fig. S4B†). In addition, the current–time signal could be retained at about 20 mA cm^{-2} for 10 h with no visible degradation, confirming remarkable long-term stability of RuPd/C (Fig. 3F). To provide insight into intrinsic activity of the catalysts, double-layer capacitance (C_{dl}) was further measured as an indicator for the electrochemically active surface area (ECSA). Fig. S5† manifests a moderate C_{dl} of RuPd/C (4.3 mF cm^{-2}) compared with that of Pt/C (6.3 mF cm^{-2}), Ru/C (3.8 mF cm^{-2}) and Pd/C (0.98 mF cm^{-2}). Thereafter, the ECSA-normalized LSV data were obtained for the HER and HzOR (Fig. S6†), which indeed reveal an obviously larger current on RuPd/C, demonstrating its better intrinsic activity for the HER and HzOR.[46,57]

3.3. Two-electrode OHzS performance

Given the outstanding bifunctional activity and superior durability on RuPd/C, a two-electrode OHzS cell was then

constructed with RuPd/C or Pt/C as both the cathode and anode to investigate the possibility of energy-saving H_2 production. As depicted in Fig. 3G, the OHzS system separately requires voltages of 17.7, 78.3 and 147.6 mV to afford 10, 50 and 100 mA cm^{-2}, far below that of Pt/C (237.9, 417.6 and 548.5 mV), while the OWS system requires voltages of 1.91, 2.26 and 2.39 V respectively to achieve the above same currents (Fig. 3H), each having a voltage difference of about 2 V with OHzS, evidently justifying huge energy-efficient superiority for OHzS. Furthermore, RuPd/C also exhibits good stability in the OHzS electrolyser without prominent current decline in 10 h (Fig. 3I), exhibiting its good prospect in practicality.

In order to explore the possibility of its practical application, a self-powered hydrogen production system for driving the OHzS device is assembled with a direct hydrazine–hydrogen peroxide fuel cell (DHHPFC) as the power, with RuPd/C as the anode and Pt/C as the cathode (Fig. 4A). As seen from Fig. 4B, the open circuit voltage (OCV) of the DHHPFC using RuPd/C||Pt/C is 1.71 V, superior to that of Pt/C||Pt/C (1.58 V). Based on the measured discharge polarization curves (Fig. 4C), the maximum power density of the DHHPFC based on RuPd/C||Pt/C can reach 108.0 mW cm^{-2}, much larger than that of Pt/C||Pt/C (56.8 mW cm^{-2}). Through the water drainage method, the hydrogen generation rate reaches 0.85 mmol h^{-1} (Fig. 4D) whereafter, the

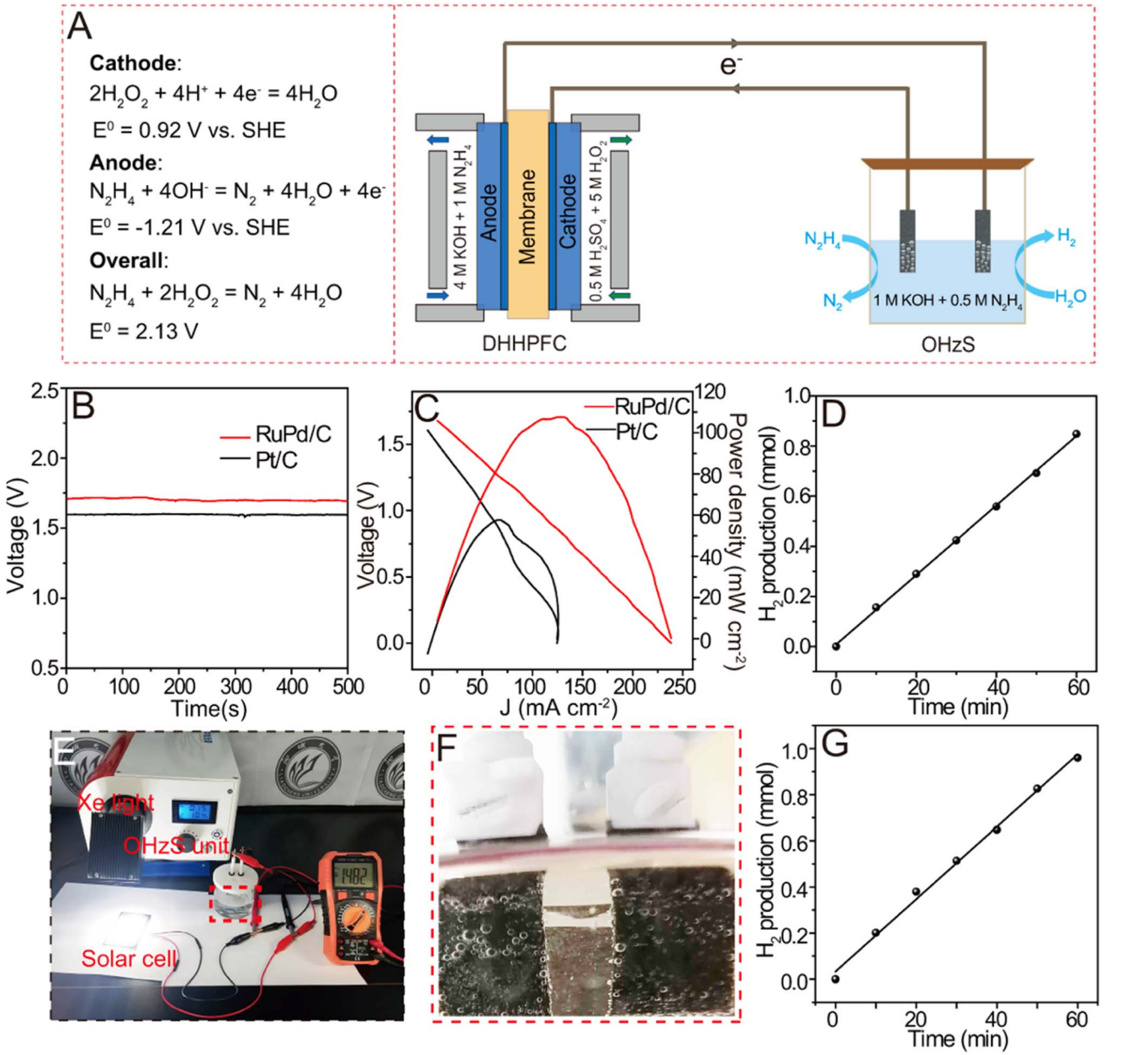

Fig. 4 (A) Schematic illustration and the working principle of the DHHPFC. (B) Open-circuit voltage of the Pt/C||Pt/C and RuPd/C||Pt/C DHHPFCs. (C) Discharge polarization curve and power density plot of the DHHPFCs. (D) The H_2 production from OHzS driven by a DHHPFC. (E) Digital photograph of the setup for OHzS driven by a solar cell. (F) Digital photograph of the evolution of gas bubbles on the solar cell-powered OHzS unit. (G) The H_2 production from the solar cell-powered OHzS unit.

feasibility of OHzS driven by the solar cell can be further proceeded with the purchased solar cell panel, which can offer a working voltage of about 1.48 V under simulated sunlight (Fig. 4E). Similarly, violent bubbles continuously escape from both electrodes of the OHzS unit (Fig. 4F) with a decent H_2 yield of 0.98 mmol h^{-1} (Fig. 4G), suggesting the feasibility of solar energy decomposition of aquatic hydrogen at the RuPd/C electrode.

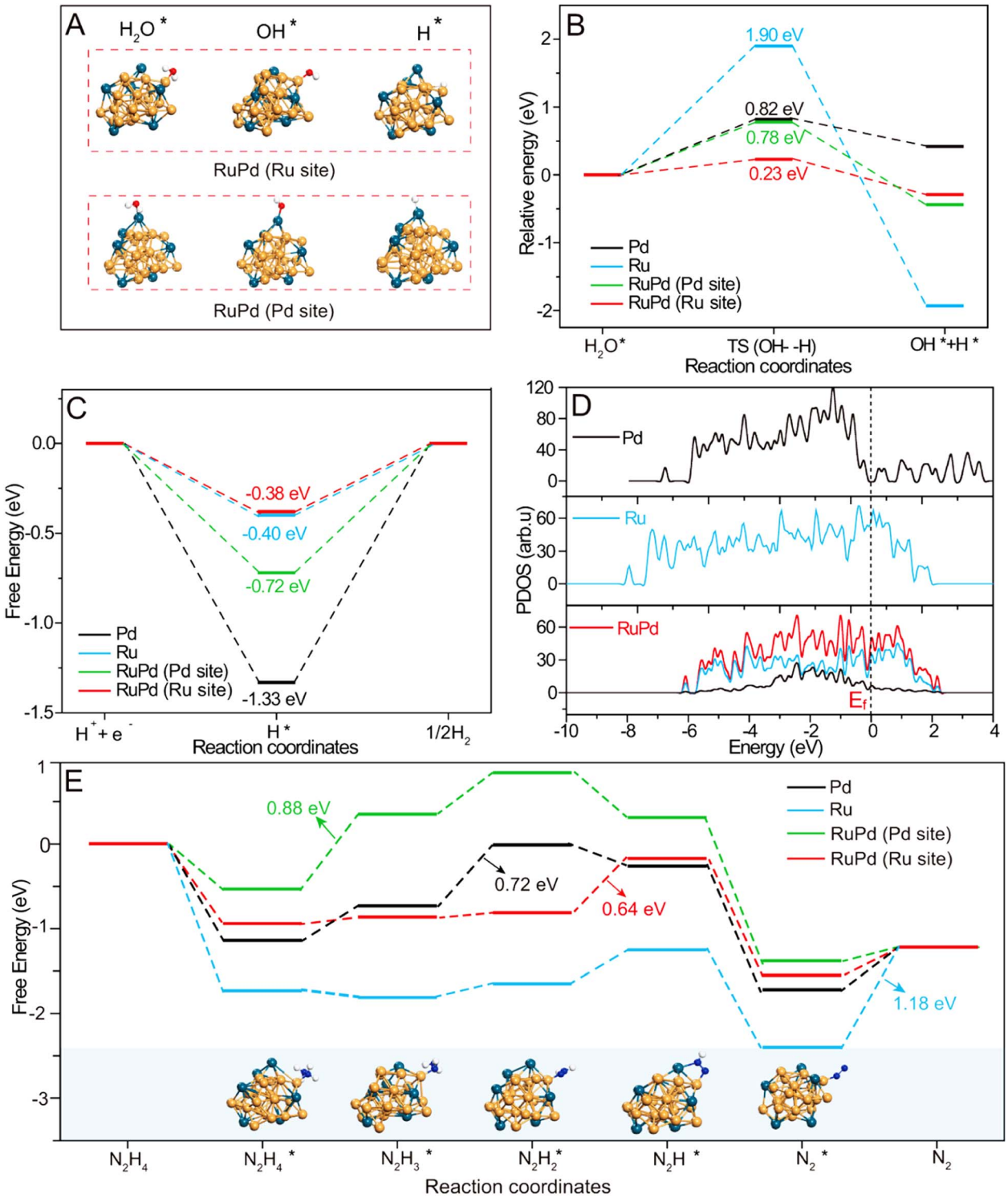

Fig. 5 (A) The side-view structural models with adsorbed H_2O*, OH* and H* on RuPd (Ru site) and RuPd (Pd site). (B) Water dissociation energy barrier and (C) ΔG_H^* on Pd, Ru, RuPd (Pd site) and RuPd (Ru site). (D) The DOSs of pure Pd, pure Ru and the RuPd alloy. (E) Reaction pathways and the free energy profiles of HzOR intermediates on the Pd, Ru, RuPd (Pd site) and RuPd (Ru site) as well as the adsorbed models of HzOR intermediates on RuPd (Ru site). The yellow, green, blue, red and white spheres represent Ru, Pd, N, O and H atoms respectively.

3.4. Mechanism investigation

To decode the underlying origin of bifunctional activity on RuPd/C, DFT calculations were further conducted. Four structural models were constructed including the pure Ru, pure Pd and RuPd alloy with Ru and Pd sites. The alkaline HER involves the initial water dissociation followed by the H ad/desorption step.[58,59] First, water dissociation energies on different models were analyzed and calculated and are shown in Fig. 5A, B and S7.† Obviously, RuPd (Ru site) has a lower energy barrier of water dissociation (0.23 eV) than that on RuPd (Pd site) (0.78 eV), bare Pd (0.82 eV) and bare Ru (1.90 eV), indicating that the Ru site on the RuPd alloy has the most favorable water dissociation kinetics. As for the H ad/desorption step, free energy of hydrogen absorption (ΔG_H^*) has been recognized as a critical indicator and the ideal ΔG_H^* should be more thermoneutral (0 eV).[58] As shown in Fig. 5C, the ΔG_H^* on RuPd (Ru site) is optimal as −0.38 eV, in comparison with pure Ru (−0.40 eV), pure Pd (−1.33 eV) and the Pd site of RuPd (−0.72 eV). The possible reason is that alloying by Pd can tune the electronic properties of Ru, thereby reducing water dissociation energies and optimizing H ad/desorption ability, which can be further verified with total density of states (DOS). As shown in Fig. 5D, the RuPd alloy possesses higher electron density near the Fermi level (E_f) than the bare Ru and Pd. Enriched DOS near E_f enabled RuPd to be more conductive with more charge carriers involved in the electrocatalytic reactions.

The alkaline HzOR involves the stepwise dehydrogenation of N_2H_4 ($N_2H_4 \rightarrow N_2H_4^* \rightarrow N_2H_3^* \rightarrow N_2H_2^* \rightarrow N_2H^* \rightarrow N_2^*$), which was also theoretically investigated over the RuPd alloy and monometal models (Fig. S8†).[60,61] As displayed in Fig. 5E, the N_2H_4 adsorption on all samples is thermodynamically spontaneous. However, the rate-determining step (RDS) varies on different models. The RDS on bare Ru is N_2 desorption with an energy barrier of 1.18 eV, while that for bare Pd is dehydrogenation of $N_2H_3^*$ to $N_2H_2^*$ with 0.72 eV. Upon alloying, the RDS on Ru and Pd sites of RuPd changes separately referring to that on bare Ru and Pd. The RuPd (Ru site) has the smallest energy barrier of 0.64 eV with the RDS from $N_2H_2^*$ to N_2H^*, while the RDS on RuPd (Pd site) is the dehydrogenation of $N_2H_4^*$ to $N_2H_3^*$ with the energy difference of 0.88 eV. Accordingly, Ru in the RuPd alloy also acts as the optimal active sites for the HzOR. Therefore, the combined experimental and theoretical studies validate that the RuPd alloy can tailor the electronic properties of Ru, resultantly effectively optimizing the water dissociation barrier and ΔG_{H^*} for the HER, and also greatly lowering the energy barrier of the RDS toward the HzOR.

4. Conclusion

In summary, a simple method was proposed to prepare tiny RuPd alloy nanoparticles uniformly loaded onto pretreated activated carbon, exhibiting outstanding bifunctional properties for alkaline HER and HzOR. Concretely, RuPd/C only demands an ultrasmall work potential of −15.3 and −77.9 mV for the HER and HzOR to afford 10 mA cm^{-2}, respectively. Particularly, an ultralow voltage of 17.7 and 147.6 mV is separately required for the OHzS system with RuPd/C at 10 and 100 mA cm^{-2}, greatly superior to the OWS system (1.9 and 2.39 V), displaying its unique energy-efficient feature. Benefitting from the remarkable HzOR activity, the self-made DHHPFC assembled with RuPd/C can afford an OCV value of 1.71 V and a power density value of 108.0 mW cm^{-2}. Moreover, the OHzS system can be readily driven by a DHHPFC and solar cell to yield substantial amounts of H_2 of 0.85 and 0.98 mmol h^{-1}, respectively. The DFT calculations reveal that Pd alloying can endow Ru active sites with a decreased water dissociation barrier and optimized ΔG_{H^*} for the HER, and a lowered energy barrier between HzOR intermediates.

Author contributions

Simeng Zhao: conceptualization, investigation, writing – original draft. Yankai Zhang: methodology, validation. Haibo Li: validation, funding acquisition. Suyuan Zeng: visualization, formal analysis. Rui Li: software. Qingxia Yao: methodology, data curation. Hongyan Chen: resources, data curation. Yao Zheng: supervision, project administration, writing – review & editing. Konggang Qu: supervision, funding acquisition, writing – review & editing.

Conflicts of interest

The authors declare no conflict of interest.

Acknowledgements

This work was financially supported by the Development Project of Youth Innovation Team in Shandong Colleges and Universities (2019KJC031), Natural Science Foundation of Shandong Province (ZR2019MB064 and ZR2021MB122) and Doctoral Program of Liaocheng University (318051608).

References

1 X. Wu, S. Zhou, Z. Wang, J. Liu, W. Pei, P. Yang, J. Zhao and J. Qiu, *Adv. Energy Mater.*, 2019, **9**, 1901333.
2 S. Chu, Y. Cui and N. Liu, *Nat. Mater.*, 2017, **16**, 16–22.
3 Q. Qian, J. Zhang, J. Li, Y. Li, X. Jin, Y. Zhu, Y. Liu, Z. Li, A. El-Harairy, C. Xiao, G. Zhang and Y. Xie, *Angew. Chem., Int. Ed.*, 2021, **60**, 5984–5993.
4 Z. Luo, H. Zhang, Y. Yang, X. Wang, Y. Li, Z. Jin, Z. Jiang, C. Liu, W. Xing and J. Ge, *Nat. Commun.*, 2020, **11**, 1116.
5 Y. Liu, J. Zhang, Y. Li, Q. Qian, Z. Li, Y. Zhu and G. Zhang, *Nat. Commun.*, 2020, **11**, 1853.
6 Z. W. Seh, J. Kibsgaard, C. F. Dickens, I. Chorkendorff, J. K. Nørskov and T. F. Jaramillo, *Science*, 2017, **355**, eaad4998.
7 Y. Huang, Q. Gong, X. Song, K. Feng, K. Nie, F. Zhao, Y. Wang, M. Zeng, J. Zhong and Y. Li, *ACS Nano*, 2016, **10**, 11337–11343.
8 Y. Guo, X. Liu, Y. Zang, Y. Wu, Q. Zhang, Z. Wang, Y. Liu, Z. Zheng, H. Cheng, B. Huang, Y. Dai and P. Wang, *J. Mater. Chem. A*, 2022, **10**, 17297–17306.

9 W.-Z. Li, M.-Y. Liu, L. Gong, M.-L. Zhang, C. Cao and Y. He, *Appl. Surf. Sci.*, 2021, **560**, 150041.
10 C. Hu, L. Zhang and J. Gong, *Energy Environ. Sci.*, 2019, **12**, 2620–2645.
11 J. Yang, L. Xu, W. Zhu, M. Xie, F. Liao, T. Cheng, Z. Kang and M. Shao, *J. Mater. Chem. A*, 2022, **10**, 1891–1898.
12 Z. Zhuang, Y. Wang, C.-Q. Xu, S. Liu, C. Chen, Q. Peng, Z. Zhuang, H. Xiao, Y. Pan, S. Lu, R. Yu, W.-C. Cheong, X. Cao, K. Wu, K. Sun, Y. Wang, D. Wang, J. Li and Y. Li, *Nat. Commun.*, 2019, **10**, 4875.
13 J. Huang, C. Du, Q. Dai, X. Zhang, J. Tang, B. Wang, H. Zhou, Q. Shen and J. Chen, *J. Alloys Compd.*, 2022, **917**, 165447.
14 K. Ojha, S. Saha, P. Dagar and A. K. Ganguli, *Phys. Chem. Chem. Phys.*, 2018, **20**, 6777–6799.
15 J. Du, D. Xiang, K. Zhou, L. Wang, J. Yu, H. Xia, L. Zhao, H. Liu and W. Zhou, *Nano Energy*, 2022, **104**, 107875.
16 T. Wang, L. Miao, S. Zheng, H. Qin, X. Cao, L. Yang and L. Jiao, *ACS Catal.*, 2023, 4091–4100.
17 T. Wang, X. Cao and L. Jiao, *Angew. Chem., Int. Ed.*, 2022, **61**, e202213328.
18 J. Wang, X. Guan, H. Li, S. Zeng, R. Li, Q. Yao, H. Chen, Y. Zheng and K. Qu, *Nano Energy*, 2022, **100**, 107467.
19 X. Guan, Q. Wu, H. Li, S. Zeng, Q. Yao, R. Li, H. Chen, Y. Zheng and K. Qu, *Appl. Catal. B Environ.*, 2023, **323**, 122145.
20 H.-L. Huang, X. Guan, H. Li, R. Li, R. Li, S. Zeng, S. Tao, Q. Yao, H. Chen and K. Qu, *Chem. Commun.*, 2022, **58**, 2347–2350.
21 Y. Li, J. Zhang, Y. Liu, Q. Qian, Z. Li, Y. Zhu and G. Zhang, *Sci. Adv.*, 2020, **6**, eabb4197.
22 J. Y. Zhang, H. Wang, Y. Tian, Y. Yan, Q. Xue, T. He, H. Liu, C. Wang, Y. Chen and B. Y. Xia, *Angew. Chem., Int. Ed. Engl.*, 2018, **57**, 7649–7653.
23 Z. Wang, L. Xu, F. Huang, L. Qu, J. Li, K. A. Owusu, Z. Liu, Z. Lin, B. Xiang, X. Liu, K. Zhao, X. Liao, W. Yang, Y.-B. Cheng and L. Mai, *Adv. Energy Mater.*, 2019, **9**, 1900390.
24 D. Khalafallah, M. Zhi and Z. Hong, *ChemCatChem*, 2021, **13**, 81–110.
25 Z. Guo, R. Wang, Y. Guo, J. Jiang, Z. Wang, W. Li and M. Zhang, *ACS Catal.*, 2022, **12**, 15193–15206.
26 F. Luo, Q. Zhang, X. Yu, S. Xiao, Y. Ling, H. Hu, L. Guo, Z. Yang, L. Huang, W. Cai and H. Cheng, *Angew. Chem., Int. Ed.*, 2018, **57**, 14862–14867.
27 Y. Yang, Y. Yu, J. Li, Q. Chen, Y. Du, P. Rao, R. Li, C. Jia, Z. Kang, P. Deng, Y. Shen and X. Tian, *Nano-Micro Lett.*, 2021, **13**, 160.
28 S. Han, Q. Yun, S. Tu, L. Zhu, W. Cao and Q. Lu, *J. Mater. Chem. A*, 2019, **7**, 24691–24714.
29 B. Xu, Y. Zhang, L. Li, Q. Shao and X. Huang, *Coord. Chem. Rev.*, 2022, **459**, 214388.
30 D. H. Kweon, M. S. Okyay, S.-J. Kim, J.-P. Jeon, H.-J. Noh, N. Park, J. Mahmood and J.-B. Baek, *Nat. Commun.*, 2020, **11**, 1278.
31 M. Zhou, C. Li and J. Fang, *Chem. Rev.*, 2021, **121**, 736–795.
32 D. Zhang, H. Zhao, B. Huang, B. Li, H. Li, Y. Han, Z. Wang, X. Wu, Y. Pan, Y. Sun, X. Sun, J. Lai and L. Wang, *ACS Cent. Sci.*, 2019, **5**, 1991–1997.
33 Q. Zou, Y. Akada, A. Kuzume, M. Yoshida, T. Imaoka and K. Yamamoto, *Angew. Chem., Int. Ed.*, 2022, **61**, e202209675.
34 Z.-P. Wu, S. Shan, S.-Q. Zang and C.-J. Zhong, *Acc. Chem. Res.*, 2020, **53**, 2913–2924.
35 H. Wang and H. D. Abruña, *J. Phys. Chem. C*, 2021, **125**, 7188–7203.
36 K. Qu, Y. Wang, A. Vasileff, Y. Jiao, H. Chen and Y. Zheng, *J. Mater. Chem. A*, 2018, **6**, 21827–21846.
37 J. Li, Y. Li, J. Wang, C. Zhang, H. Ma, C. Zhu, D. Fan, Z. Guo, M. Xu, Y. Wang and H. Ma, *Adv. Funct. Mater.*, 2022, **32**, 2109439.
38 M. Tang, S. Mao, M. Li, Z. Wei, F. Xu, H. Li and Y. Wang, *ACS Catal.*, 2015, **5**, 3100–3107.
39 J. Mahmood, F. Li, S.-M. Jung, M. S. Okyay, I. Ahmad, S.-J. Kim, N. Park, H. Y. Jeong and J.-B. Baek, *Nat. Nanotechnol.*, 2017, **12**, 441–446.
40 K. Qu, Y. Zheng, X. Zhang, K. Davey, S. Dai and S. Z. Qiao, *ACS Nano*, 2017, **11**, 7293–7300.
41 R. M. Mironenko, O. B. Belskaya, T. I. Gulyaeva, M. V. Trenikhin, A. I. Nizovskii, A. V. Kalinkin, V. I. Bukhtiyarov, A. V. Lavrenov and V. A. Likholobov, *Catal. Today*, 2017, **279**, 2–9.
42 A. Mitra, D. Jana and G. De, *Ind. Eng. Chem. Res.*, 2013, **52**, 15817–15823.
43 J. Tan, J. Cui, Y. Zhu, X. Cui, Y. Shi, W. Yan and Y. Zhao, *ACS Sustainable Chem. Eng.*, 2019, **7**, 10670–10678.
44 Y.-T. Li, X.-L. Zhang, Z.-K. Peng, P. Liu and X.-C. Zheng, *Fuel*, 2020, **277**, 118243.
45 Q. Yang, B. Zhu, F. Wang, C. Zhang, J. Cai, P. Jin and L. Feng, *Nano Res.*, 2022, **15**, 5134–5142.
46 J. Li, C. Zhang, C. Zhang, H. Ma, Y. Yang, Z. Guo, Y. Wang and H. Ma, *Chem. Eng. J.*, 2022, **430**, 132953.
47 N. Jia, Y. Liu, L. Wang, P. Chen, X. Chen, Z. An and Y. Chen, *ACS Appl. Mater. Interfaces*, 2019, **11**, 35039–35049.
48 J. Shi, Q. Sun, W. Zhu, T. Cheng, F. Liao, M. Ma, J. Yang, H. Yang, Z. Fan and M. Shao, *Chem. Eng. J.*, 2023, **463**, 142385.
49 Y. Jeong, S. Shankar Naik, Y. Yu, J. Theerthagiri, S. J. Lee, P. L. Show, H. C. Choi and M. Y. Choi, *J. Mater. Sci. Nanotechnol.*, 2023, **143**, 20–29.
50 M. Zhang, Z. Wang, Z. Duan, S. Wang, Y. Xu, X. Li, L. Wang and H. Wang, *J. Mater. Chem. A*, 2021, **9**, 18323–18328.
51 X. Fu, D. Cheng, C. Wan, S. Kumari, H. Zhang, A. Zhang, H. Huyan, J. Zhou, H. Ren, S. Wang, Z. Zhao, X. Zhao, J. Chen, X. Pan, P. Sautet, Y. Huang and X. Duan, *Adv. Mater.*, 2023, 2301533.
52 W. Tian, X. Zhang, Z. Wang, L. Cui, M. Li, Y. Xu, X. Li, L. Wang and H. Wang, *Chem. Eng. J.*, 2022, **440**, 135848.
53 X. Liu, T. Wang, Y. Chen, J. Wang, W. Xie, R. Wu, X. Xu, L. Pang, X. Zhang, Y. Lv, G. Wang, Y. Yamauchi and T. Jin, *Appl. Catal. B Environ.*, 2023, **333**, 122771.
54 Y. Liu, J. Zhang, Y. Li, Q. Qian, Z. Li and G. Zhang, *Adv. Funct. Mater.*, 2021, **31**, 2103673.
55 J.-Y. Zhang, H. Wang, Y. Tian, Y. Yan, Q. Xue, T. He, H. Liu, C. Wang, Y. Chen and B. Y. Xia, *Angew. Chem., Int. Ed.*, 2018, **57**, 7649–7653.

56 Q. Qian, Y. Li, Y. Liu, Y. Guo, Z. Li, Y. Zhu and G. Zhang, *Chem. Eng. J.*, 2021, **414**, 128818.
57 J. Li, Q. Zhou, C. Zhong, S. Li, Z. Shen, J. Pu, J. Liu, Y. Zhou, H. Zhang and H. Ma, *ACS Catal.*, 2019, **9**, 3878–3887.
58 Q. Yu, J. Chi, G. Liu, X. Wang, X. Liu, Z. Li, Y. Deng, X. Wang and L. Wang, *Sci. China Mater.*, 2022, **65**, 1539–1549.
59 F. Sun, Q. Tang and D.-e. Jiang, *ACS Catal.*, 2022, **12**, 8404–8433.
60 F. Sun, J. Qin, Z. Wang, M. Yu, X. Wu, X. Sun and J. Qiu, *Nat. Commun.*, 2021, **12**, 4182.
61 Y. Zhu, J. Zhang, Q. Qian, Y. Li, Z. Li, Y. Liu, C. Xiao, G. Zhang and Y. Xie, *Angew. Chem., Int. Ed.*, 2022, **61**, e202113082.